CrossMark

Cobalt Sulfide/Reduced Graphene Oxide Nanocomposite with Enhanced Performance for Supercapacitors

JIA ZHU,[1,2] WENTAO ZHOU,[2] YAZHOU ZHOU,[1] XIAONONG CHENG,[1] and JUAN YANG ![ORCID][1,3]

1.—School of Materials Science and Engineering, Jiangsu University, Zhenjiang 212013, People's Republic of China. 2.—School of Environmental and Chemical Engineering, Jiangsu University of Science and Technology, Zhenjiang 212003, People's Republic of China. 3.—e-mail: yangjuan6347@ujs.edu.cn

A cobalt sulfide decorated reduced graphene oxide (CoS/rGO) nanocomposite was successfully synthesized via a facile one-step hydrothermal route assisted by ethylenediamine. The crystalline phase, structure and morphology of the products were systematically characterized by x-ray diffraction, transmission electron microscopy, scanning electron microscopy, x-ray photoelectron spectroscopy, nitrogen (N_2) absorption–desorption isotherm, Raman spectra and thermogravimetric analysis. The results show that CoS nanoparticles with the size of 30–100 nm are well dispersed on or anchored in the creasy rGO sheets substrate. Combining the CoS compound nature with the rGO outstanding characteristics, the as-obtained CoS/rGO as an electrode for a supercapacitor harvests high specific capacitance, excellent long-cycle stability and remarkable high-rate capability, which are all superior to those of pristine CoS. Importantly, this nanocomposite possesses a specific capacitance of 813 F g^{-1} at 0.5 A g^{-1} (about 2 times that of pure CoS) and excellent cycling stability with 91.2% capacitance retention after 1000 repetitive charge–discharge cycles. It is noteworthy that this approach can be readily applicable to the nanoparticle decoration of graphene sheets and the preparation of other graphene-based nanocomposites for supercapacitors.

Key words: Cobalt sulfide, reduced graphene oxide, nanocomposite, supercapacitors

INTRODUCTION

Supercapacitors or electrochemical capacitors (ECs) have been investigated as promising energy conversion and storage devices due to their ultrafast recharge ability, long lifespan, high energy density and power density.[1–4] There are two categories of ECs generally classified on the basis of their charge storage mechanism. One is pseudocapacitors dominated by Faradic processes of active electrode material, and the other is electrical double-layer capacitors (EDLCs) which rely on charge accumulation at the electrode/electrolyte surface.[5]

Compared with non-Faradic reactions in EDLCs, pseudocapacitors are governed by a reversible Faradic reaction of electroactive material and thus deliver a high specific capacitance.[6,7]

Cobalt sulfide with various stoichiometric compositions (e.g., CoS, CoS_2, Co_3S_4, Co_8S_9) has been widely explored for energy conversion and storage systems. Specifically, CoS is regarded as an auspicious candidate for supercapacitors owing to its high reversible redox capability and cost effectiveness.[8–10] Nevertheless, CoS electrode materials are still plagued by drawbacks arising from their pulverization during the electrochemical process, such as poor electrical conductivity, limited specific capacitance, fast capacity decay and low rate property.[11–13] Consequently, many researchers have focused on the rational designing of desirable

materials with special nanostructures and novel developing composites at the nanoscale to address these issues.[14–16] In particular, an effective strategy of introducing a carbonaceous material substrate has been extensively employed to generate electroactive materials with improved capacitive performance[17–19] Graphene, a single-layer two-dimensional (2D) nanosheet of graphite, is a promising material for supercapacitors due to its unique features such as high conductivity, excellent mechanical flexibility and chemical innerness. Currently, reduced graphene oxide (rGO) is a general graphene derivative, which has been widely utilized as the substrate in rGO-based nanocomposites to reinforce the electrochemical properties in comparison with the counterparts in the absence of rGO. Previous studies have investigated CoS/rGO nanocomposites for their applications in supercapacitors. For instance, β-cobalt sulfide nanoparticles decorated graphene composite electrodes are obtained via hydrothermal treatment and an Ar calcination approach.[20] CoS nanosheet/graphene composite networks on nickel foam through a two-step electrochemical deposition process encompass the performance of high specific capacitance and excellent rate capability.[21] A CoS/rGO hybrid composite with rGO layers and CoS nanoparticles can only deliver 550 F g^{-1} at 1 A g^{-1}.[22] Supercapacitors made of a 3D graphene/CoS$_x$ composite with low crystallinity of CoS$_x$ nanoflakes exhibit 443 F. g^{-1} at 1 A g^{-1}.[23] Although many efforts have been made to produce cobalt sulfide/rGO nanocomposites as supercapacitors, these composites are still hindered by the problems of a tedious synthesis procedure, additional cost, limited specific capacitance and poor crystallinity of cobalt sulfide. Hence, a simple, efficient, and cost-effective means of acquiring cobalt sulfide/rGO nanocomposites with excellent electrochemical properties for supercapacitors is desirable.

Here, we report a facile one-step hydrothermal method to fabricate a CoS/rGO nanocomposite in the presence of ethylenediamine. During the process, the reduction of GO sheets to rGO and *in situ* embedding of CoS nanoparticles into GO sheets occurs simultaneously, leading to the formation of a CoS/rGO nanocomposite. Benefiting from the synergistic effects of the CoS compound nature and the rGO characteristics, the CoS/rGO electrode as a supercapacitor presents typical pseudocapacitance behaviors with a high specific capacitance of 813 F g^{-1} at 0.5 A g^{-1} (about twofold that of CoS), a remarkable rate capability and an excellent cycling durability of 91.2% specific capacitance retention after 1000 cycles, which offers potential applications of rGO-based nanocomposites in supercapacitors. In addition, the mass ratio of Co(CH$_3$COO)$_2$·4H$_2$O to GO has a remarkable influence on the pseudocapacitance properties of the CoS/rGO nanocomposite, suggesting that a suitable loading

content of CoS on rGO is essential for optimal electrochemical properties.

EXPERIMENTAL

Materials and Chemicals

All chemicals were purchased commercially from Sinapham Chemical Reagent (Shanghai, China). Nickel foam, acetylene black and polytetrafluoroethylene (PTFE) were bought from Lizhiyuan Electronics (Taiyuan, China). All materials and chemical reagents were of analytical grade and used as received. Deionized water with a resistivity of 18 MΩ was used in each experiment.

Preparation of CoS/rGO

GO was attained from graphite powders by a modified Hummers' method, as previously reported.[24,25] A GO aqueous dispersion (3 mg mL^{-1}) was obtained by ultrasonicating the as-synthesized GO sheets in water for 1 h under ambient conditions. A series of CoS/rGO nanocomposites with different component ratios of CoS to rGO were synthesized. Here, the weight content of CoS was controlled by adjusting the mass ratio (r) of Co(CH$_3$COO)$_2$·4H$_2$O to GO. CoS/rGO with $r = 6$ was fabricated as follows: Co(CH$_3$COO)$_2$·4H$_2$O (0.36 g) and thiourea (0.218 g) were firstly dissolved in 20 mL GO aqueous dispersion (3 mg mL^{-1}). The dispersion was then homogeneously stirred for 30 min. Next, 300 μL ethylenediamine was added to the mixture. After 1 h of vigorous stirring, the mixture was transferred to a 25-mL Teflon-lined autoclave for hydrothermal processing at 180°C for 12 h. After cooling to room temperature, the black product was separated via filtration, rinsing, and centrifugation with water and absolute ethanol. The final product (denoted as CoS/rGO) was acquired after vacuum drying overnight at 60°C. In comparison, pure CoS was prepared by the same hydrothermal treatment as CoS/rGO in the absence of GO.

Materials Characterizations

The microstructure and morphology of the obtained materials were observed via scanning electron microscopy (SEM; JEOL 7800f) equipped with energy dispersive spectroscopy (EDS; Oxford) and transmission electron microscopy (TEM; JEOL 2010) at an accelerating voltage of 200 kV. The crystal structure was determined by means of powder x-ray diffraction with Cu Kα radiation (XRD; Rigaku Dmax 2500 PC). The specific surface area, calculated using the Brunauer–Emmett–Teller (BET) method, was taken on a N$_2$ adsorption–desorption analyzer (ASAP 2020) at 77 K. Raman spectroscopy was performed at 532 nm on a Thermo Fisher DXR Raman spectrometer. The binding characteristics of the material were examined via x-ray photoelectron spectroscopy (XPS;

Thermo Scientific ESCALAB 250Xi) with a 1486.6-eV x-ray from Al Kα line. Thermogravimetric analysis (TGA; Perkin Elmer Pyris Diamond) was recorded at a heating rate of 10°C min^{-1} under air atmosphere.

Electrochemical Measurements

To assess the electrochemical performances of the resultant CoS/rGO, a classic three-electrode electrochemical system including the electrolyte of 6 M KOH aqueous solution was applied. CoS/rGO-modified electrode was achieved by combining 80 wt.% CoS/rGO, 10 wt.% acetylene black with 10 wt.% PTFE binder into a slurry. The slurry was thoroughly mixed, loaded onto Ni foam (1 cm $\times$ 1 cm), and then pressed at 10 MPa. After vacuum drying at 80°C for 10 h, wa orking electrode based on a CoS/rGO-modified electrode was obtained. The mass of the electroactive material loading on Ni foam was approximately 1.5 mg. A platinum foil and a saturated calomel electrode acted as the counter and the reference electrode. The electrochemical determinations containing cyclic voltammetry (CV), galvanostatic charge/discharge (GCD) and electrochemical impedance spectroscopy (EIS) were tested on a CHI760E electrochemical work station (Shanghai, China). Cycling performance was measured with a CT 2001A Tester (Wuhan, China). The specific capacitance by GCD measurement can be calculated from Eq. 1[6]:

$$C = I \cdot \Delta t / (m \cdot \Delta V) \qquad (1)$$

where C (F g^{-1}) is the specific capacitance, I (A) the constant discharging current, Δt (s) the discharge time, ΔV (V) the potential interval, and m (g) the mass of electroactive material in the electrode.

RESULTS AND DISCUSSION

Structural Characterization

The crystalline phase and structure compositions of CoS/rGO and the bare CoS sample were characterized by XRD. As the XRD patterns reveal in Fig. 1a, four typical diffraction peaks at $2\theta = 30.6°$, 35.3°, 46.9°, and 54.4° can unambiguously be assigned to the respective (100), (101), (102) and (110) phase planes of CoS. The diffraction peaks are all well-matched to the standard hexagonal CoS (lattice constants of $a = b = 3.368$ Å and $c = 5.17$ Å, JCPDS No. 65-3418). No characteristic peaks from other phases were detected, implying the high purity of both products. Moreover, a broad diffraction peak at $2\theta = 25°$ corresponding to the (002) plane of graphene is barely discernible in the XRD pattern of CoS/rGO, oossibly twing po the weak diffraction intensity of the graphene component.[26,27]

The carbon structures of GO, rGO, and CoS/rGO were investigated via Raman spectroscopy. The two peaks in Fig. 1b located at ~ 1346 cm^{-1} and ~ 1583 cm^{-1} are attributed to the D band (due to the vibrations of sp^3-bonded carbon atoms of defects in the aromatic rings) and the G band (related to the stretching of sp^2-bonded carbon atoms in rings and chains), respectively.[28] For rGO and CoS/rGO, the peak of each band will in general move slightly to a lower Raman shift than the peaks for GO after GO has been reduced to rGO.[29] Values of 1.14. 0.92, and 1.13 are calculated for the respective D/G peak intensity ratios (I_D/I_G) of CoS/rGO, GO, and rGO. This indicates that (1) compared with the graphene sheets in GO, graphene sheets in CoS/rGO contain fewer disorders and defects, and (2) GO is partially reduced during the hydrothermal fabrication of
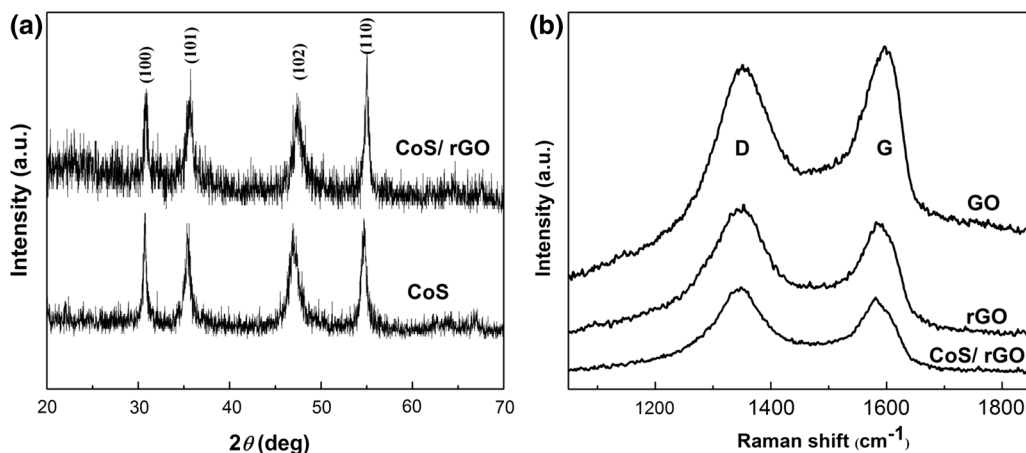

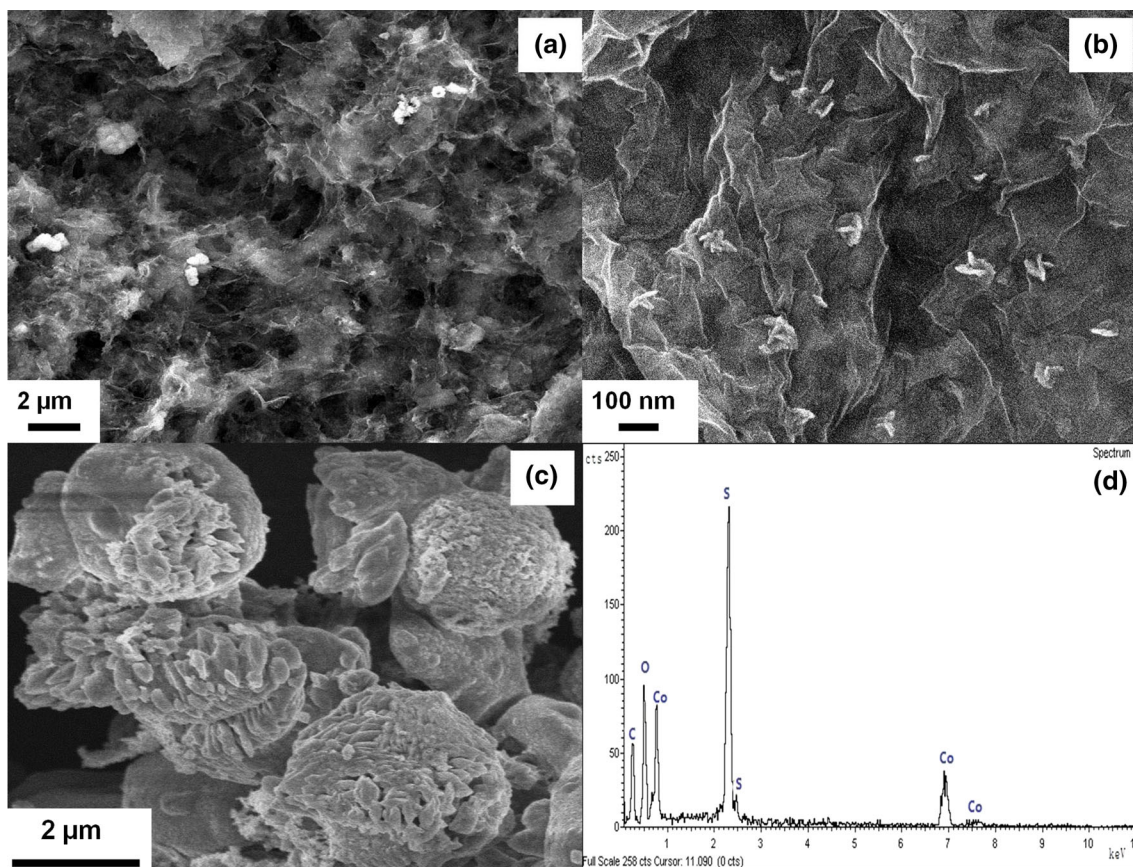Fig. 1. (a) XRD patterns of CoS and CoS/rGO; (b) Raman spectra of GO, rGO and CoS/rGO.

Fig. 2. SEM images at different magnifications of (a, b) CoS/rGO and (c) CoS; (d) EDS pattern of CoS/rGO.

CoS/rGO. The I_D/I_G of CoS/rGO is higher than that of GO, owing to a decrease in the disordered restacking extent of graphene sheets originating from partial CoS-nanoparticle incorporation into the layer-by-layer structures of rGO.[20]

The morphology and microstructure of the bare CoS sample and CoS/rGO were investigated via SEM. Typical high-magnification SEM images in Fig. 2a and b reveal that CoS nanoparticles with a broad size distribution (30–100 nm) are uniformly embedded in, wrapped in or loaded on wrinkled and restacked graphene sheets. In strong contrast, the pure CoS product in the absence of rGO is composed of quasi-flower-like microspheres (see Fig. 2c), which are constructed by two-dimensional cross-linked and stacked CoS nanopetals. The morphology of the pure CoS sample is significantly different from that of the CoS nanoparticles in CoS/rGO. The large particle size and condensed microstructure of the pure product suggest that the introduction of rGO as a supporting substrate in CoS/rGO alleviates the severe aggregation of CoS particles. This promotes the formation of smaller CoS particles in the nano scale and a looser structure of CoS/rGO. The EDS spectrum (see Fig. 2d) reveals that CoS/rGO consists of only Co, S, C and O, where O is generated by the unreduced oxygen atoms in the hydroxyl and epoxy groups of the rGO substrate.

The structure of CoS/rGO was further investigated via TEM. Typical images at various magnifications are shown in Fig. 3. The images (see Fig. 3a) show that highly-dispersed CoS nanoparticles are homogenously attached to the surface and edge of the rGO. Even after preparation of CoS/rGO for the TEM sample via ultrasonication in ethanol, these nanoparticles are still strongly anchored in the rGO, signifying the tight binding between the nanoparticles and the graphene sheets. Meanwhile, microsized CoS free particles are completely absent. In good accordance with the SEM analysis, the high-magnification TEM image shown in Fig. 3b discloses that the CoS nanoparticles (diameter: 30–100 nm) have non-uniform and irregular morphologies. The rGO exhibits loose layer-by-layer restacking and folding architecture with many creased sheets at the edges.

XPS tests were performed to elucidate the chemical composition of the CoS/rGO. As the survey spectrum shows in Fig. 4a, C, S, O, Co and N are the dominant elements in CoS/rGO. The N peak at 399.5 eV results from thiourea decomposition.[30] Figure 4b exhibits the high-resolution C 1s XPS spectra. Four deconvoluted peaks of C 1s at 284 eV, 285.3 eV, 286.5 eV, and 289 eV can be indexed to C=C, C-OH, C-O-C, and C=O, respectively.[26,31] In the Co 2p spectrum (see Fig. 4c), the main peak
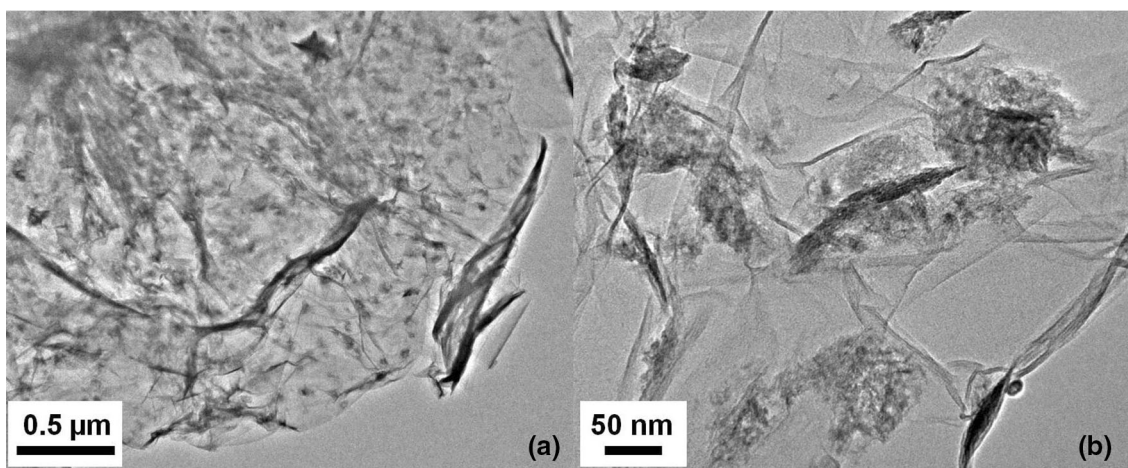
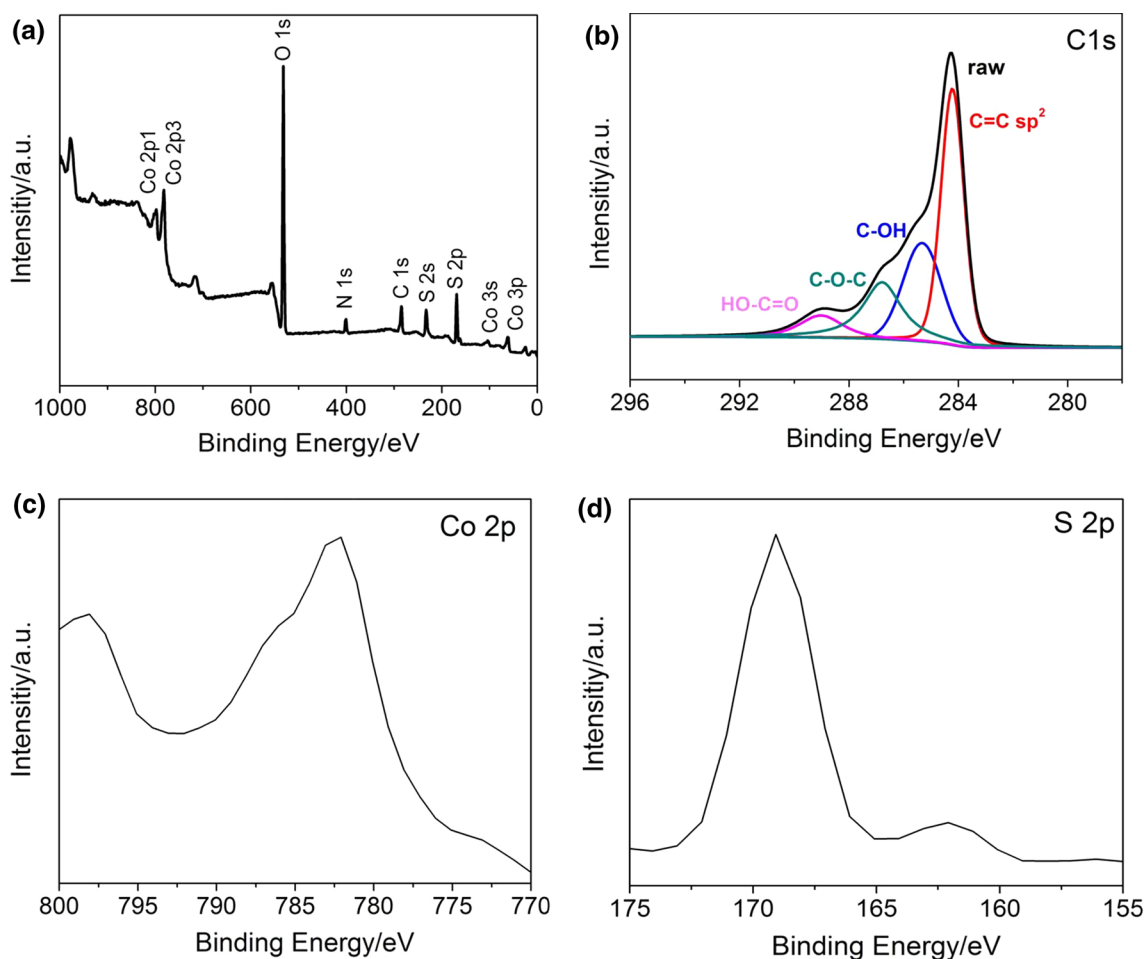Fig. 3. (a, b) TEM images of CoS/rGO obtained at two magnifications.

Fig. 4. The survey (a) and the corresponding high-resolution XPS spectra of (b) C 1s; (c) Co 2p and (d) S 2p of CoS/rGO.

centered at 782.1 eV and a shoulder peak at 798 eV are associated with the Co 2$p_{1/2}$ and Co 2$p_{3/2}$ spin–orbit couple of CoS.[32] The S 2p spectrum in Fig. 4d presents the binding energies located at 162 eV and 169 eV, which correspond to the spin–orbit peaks of S 2$p_{3/2}$ and S 2$p_{1/2}$, respectively. The S 2p signal at

162 eV indicates the existence of S^{2-} in the CoS/rGO and the binding energy of Co-S.[33] Based on the XPS analysis, we can confirm that CoS was successfully anchored in the rGO.

Figure 5a shows the N$_2$ adsorption–desorption isotherms of bare CoS and CoS/rGO. A
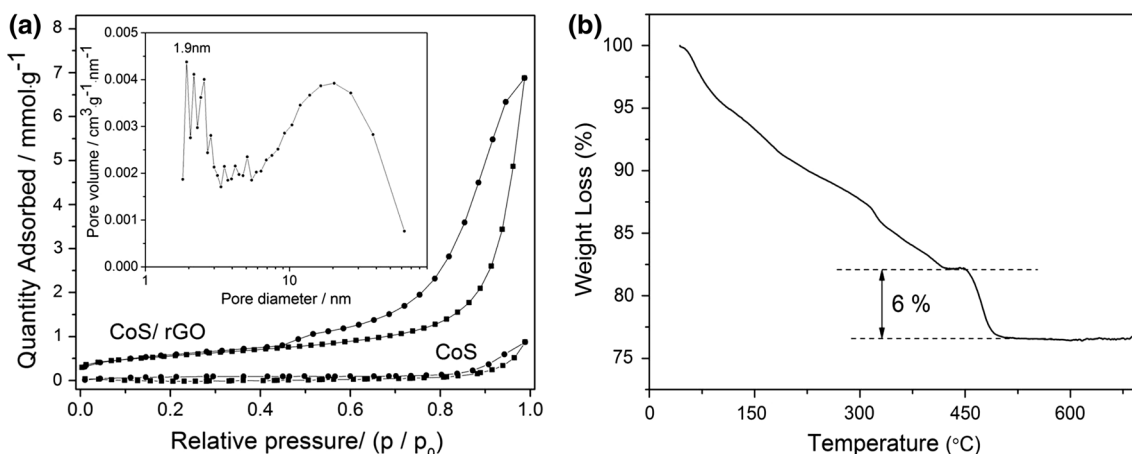
Fig. 5. (a) N$_2$ absorption–desorption isotherm of pure CoS sample and CoS/rGO (inset pore size distribution of CoS/rGO); (b) TG curve of CoS/rGO.
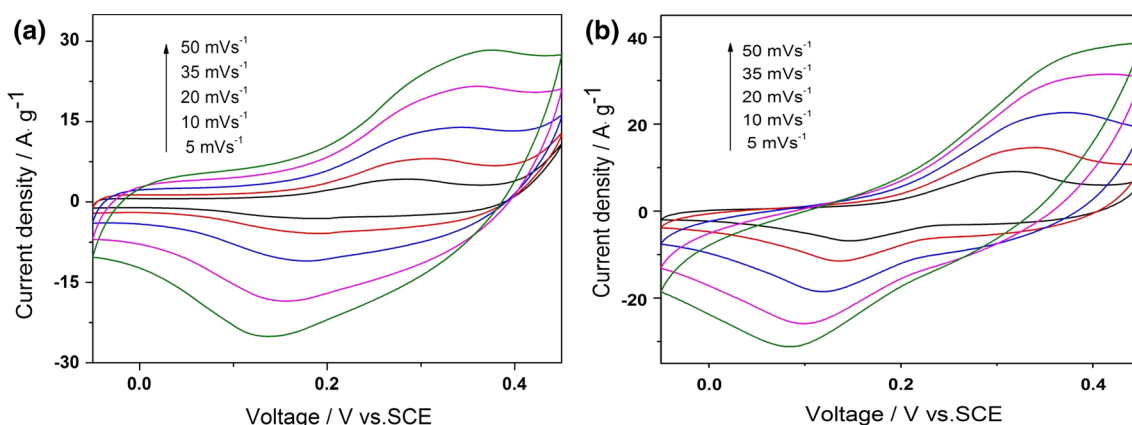

Fig. 6. CV curves of (a) pure CoS sample and (b) CoS/rGO at different sweep rates.

representative IV isotherm with an apparent hysteresis loop at various relative pressures (P/P_0) is present in both plots. Values of 44.09 m^2 g^{-1} and 0.23 cm^3 g^{-1} are determined for the BET surface area and the total pore volume of CoS/rGO, respectively. These values are considerably higher than those of pure CoS (0.176 m^2 g^{-1} and 0.03 cm^3 g^{-1}), verifying that the presence of rGO in CoS/rGO enhances the specific surface area and yields a loose structure. The weight composition of graphene in CoS/rGO is quantified through a TGA test. Stages of weight loss, consistent with those reported in previous studies,[34] are observed (see Fig. 5b). The weight loss stage at temperatures lower than 420°C can be assigned to the conversion of CoS to cobalt oxide. At ∼ 500°C, a significant weight loss occurs, confirming the burning of graphene sheets. The weight content of the graphene and CoS in CoS/rGO is estimated to be 6% and 94%, respectively.

Electrochemical Analysis

Figure 6a and b illustrates the CVs of pure CoS and CoS/rGO in the potential window of − 0.05–

0.45 V at various sweep rates. It is noted that both CV curves consist of a pair of strong redox peaks, indicating the typical pseudocapacitive features depending on Faradaic reactions occurring in the electrochemical conversions. The shape of both CV curves differs from that of EDLC, whose CV curve presents a close rectangular model.[35] The pair of redox peaks probably refer to the reversible reactions of CoS ⇋ CoSOH and CoSOH ⇋ CoSO. According to the previous results,[36,37] two electrochemical redox reactions of the CoS pseudoactive electrode in KOH aqueous electrolyte can be assumed as follows:

$$CoS + OH^- \leftrightharpoons CoSOH + e^-, \qquad (2)$$

$$CoSOH + OH^- \leftrightharpoons CoSO + H_2O + e^-. \qquad (3)$$

Sweep rate alone with the inner structure of electrode also affects the locations of redox peaks.[38] Upon the sweep rate varying from 5 mV s^{-1} to 50 mV s^{-1}, the shapes of both CV curves are retained and the potentials of the anodic and

cathodic peaks shift slightly to more positive and negative directions, respectively. This may be because the internal diffusion resistance of the supercapacitor material augments the increasing sweep rate.[39,40] Meanwhile, the peak current densities increase with the rise of the sweep rate. This phenomenon could be ascribed to the limiting charge transfer step in the Faradic reactions.[41,42] These results show that the OH^- diffusion-controlled redox reaction is predominant within the electrode. The specific capacitance simply estimated from the voltammetric method is proportional to the average area surrounded by a CV curve, and one can safely conclude that the specific capacitance of CoS/rGO is significantly higher than that of pure CoS within the same potential range.[43]

GCD profiles of pure CoS and CoS/rGO at different current densities are disclosed in Fig. 7a and b. There exists an apparent plateau and a non-linear relationship of potentialtime in GCD curves, further confirming the pseudocapacitive behaviors coming from the reversible Faradic processes between the CoS electrode and the KOH aqueous electrolyte. This result is well consistent with the analysis from

the CV curves. The specific capacitances of pure CoS and CoS/rGO calculated via GCD curves are plotted in Fig. 7c. CoS/rGO delivers the maximum specific capacitance of 813 F g^{-1} at 0.5 A g^{-1}, which approaches 1.96 times the value of pure CoS (414 F g^{-1}).

The rate capability is a crucial parameter of electrode in application for supercapacitors. Impressively, the CoS/rGO electrode still offers 489 F g^{-1} at a high current density of 10 A g^{-1}, maintaining almost 60.1% specific capacitance at 0.5 A g^{-1}. However, pure CoS only releases 148 F g^{-1} at 10 A g^{-1}, which merely covers approximately 35.7% of the value at 0.5 A g^{-1}. This evident distinction approves that as to rate capability CoS/rGO outperforms pure CoS.

The mass ratio (r) of $Co(CH_3COO)_2 \cdot 4H_2O$ to GO greatly affects the electrochemical performances of CoS/rGO nanocomposites for supercapacitors. As reflected in Fig. 7d, when $r = 0$, 2, 4, 6, and 8, the calculated specific capacitances for the CoS/rGO nanocomposite are 102 F g^{-1}, 236 F g^{-1}, 581 F g^{-1}, 813 F g^{-1} and 687 F g^{-1}, respectively Apparently, the CoS/rGO nanocomposite with $r = 6$ has the
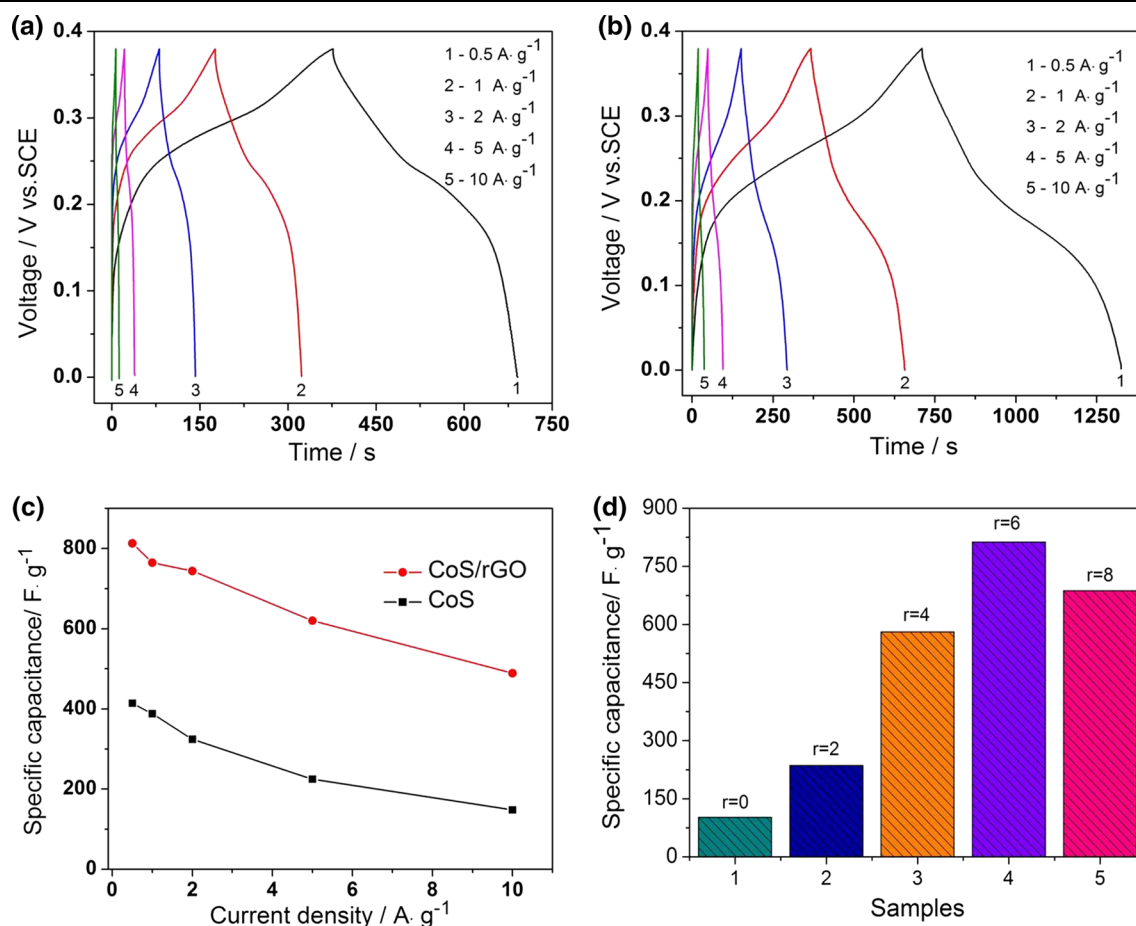

Fig. 7. GCD curves of (a) pure CoS sample and (b) CoS/rGO at different current densities from 0.5 A g^{-1} to 10 A g^{-1}; (c) Specific capacitances of CoS sample and CoS/rGO at different current densities; (d) Specific capacitances of CoS/rGO nanocomposites with different mass ratios of $Co(CH_3COO)_2 \cdot 4H_2O$ to GO.

maximal specific capacitance. Meanwhile, the values of specific capacitance first increase with the rising r, but then reduce when r is over 6. In fact, the elevated loading content of CoS on the rGO support will inevitably decrease the amount of the corresponding component rGO, and accordingly the conductivity of CoS/rGO nanocomposites declines, resulting in the drop in the specific capacitance value. Thus, an appropriate loading amount of CoS on rGO is critical for optimal electrochemical properties.

To obtain insight into the electrochemical mechanism of pure CoS and the CoS/rGO electrode, we undertook EIS measurements at open circuit potential with a fixed ac perturbation of 5 mV in the frequency range of 0.1 Hz–10 kHz. The Nyquist plots of pure CoS and CoS/rGO are shown in Fig. 8a. In both EIS spectra, a small semicircle in the high-frequency region followed by a straight line in the low-frequency region can be seen. From the equivalent circuit (inset of Fig. 8a), the point of intersection with the x-axis of the impedance plot corresponds to solution resistance (R_S), a total resistance of the inner electrode resistance, bulk electrolyte resistance, and the contact resistance between the electrolyte and the electrode. The R_S value of CoS/rGO (0.19 Ω) is dramatically smaller than that of CoS (1.02 Ω), confirming that the introduction of the rGO conducting substrate has reduced the inner electrode resistance and contact resistance, which allows efficient access for the electrolyte to the electrode surface.[44] The span of the semicircle along the x-axis represents interfacial charge-transfer resistance (R_{ct}), which is associated with the charge-transfer kinetics of the electrode in the electrolyte. Under careful observation from the magnified ESI data, CoS/rGO has a little smaller R_{ct} compared with CoS. Actually the smaller R_{ct} value is favorable for higher specific capacitance.[45] The linear part in the EIS data reflects Warburg resistance (W) mainly involving the ion diffusion process between the electrode and the electrolyte. The

higher slope of CoS/rGO manifests faster ion transport rates from the electrolyte to the electrode interface. Additionally, CoS/rGO shows a more vertical line than CoS, suggesting a more ideal pseudpcapacitor model.[46] The above EIS results cogently verify that CoS/rGO compared to CoS imparts superiority in ion transport rates and electrochemical kinetics, thus exhibiting enhanced performance for supercapacitors.[47]

Figure 8b shows the electrochemical cyclic stability of pure CoS and CoS/rGO for 1000 repetitive galvanostatic charging–discharging cycles at a constant current density of 0.5 A g^{-1}. After being cycled for 1000 cycles, the pristine CoS electrode affords a specific capacitance of 337 F g^{-1} with only 81.4% retention of its original value, while CoS/rGO displays 742 F g^{-1}, which is about an 8.8% capacitance reduction of its maximum value. Obviously, in terms of cycling properties, the CoS/rGO is superior to pure CoS.

In contrast with the reported CoS supercapacitor with limited specific capacitance, such as CoS nanoparticles (41 F g^{-1}),[48] CoS thin films (252 F g^{-1})[49] and CoS nanosheets (318 F g^{-1}),[50] our CoS/rGO could deliver 813 F g^{-1}. Moreover, CoS/rGO showed excellent cycling performance with 91.2% capacitance retention after 1000 charge—discharge cycles, while only 66% initial specific capacitance was retained for the CoS$_2$ micro-ellipsoids with tube-like cavities when being cycled for 1000 times.[11]

These advantageous electrochemical performances of CoS/rGO for supercapacitors could be attributed to beneficial synergistic effects from CoS and rGO. Firstly, graphene as a conducting agent significantly increases the electrical conductivity of CoS/rGO, and thus reduces the inner resistance of the whole electrode.[51] Secondly, highly-dispersed CoS nanoparticles in the rGO substrate can effectively avoid their agglomeration and provide enough efficient contact sites for electrochemical redox reactions between the CoS and hydrate ions.
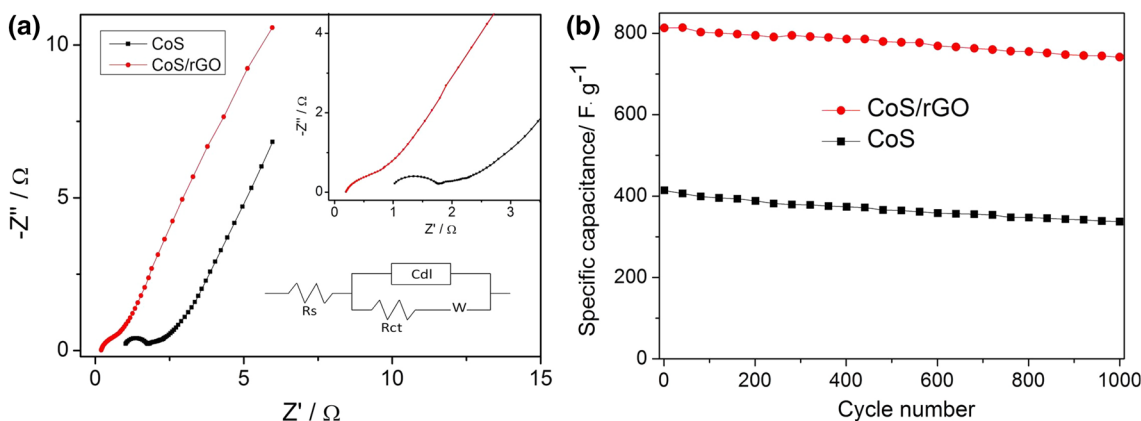

Fig. 8. (a) Nyquist plots for of CoS and CoS/rGO. *Insets* magnified plots in the high-frequency region and the equivalent circuit used to simulate the Nyquist plots; (b) cycling performance of CoS/rGO and pure CoS at 0.5 A g^{-1}.

Thirdly, the high specific area of CoS/rGO brings about excellent interfacial contact between the CoS and the graphene, improving accessible pathways for electrolyte ions and efficient ion diffusion.[52]

CONCLUSION

In summary, this work has demonstrated a facile strategy for a one-step hydrothermal process of CoS/rGO and contrastiing pristine CoS promoted by ethylenediamine. CoS nanoparticles with a broad size distribution are uniformly anchored on wrinkled and restacking rGO sheets. Benefiting from the synergistic effects between the two components of CoS and rGO, the CoS/rGO-based supercapacitor harvests a maximum specific capacitance of 813 F g^{-1} at 0.5 A g^{-1} (about 2 times that of pure CoS) and 91.2% capacitance retention of its initial value after continuous charging–discharging 1000 cycles, displaying superior specific capacitance, cycling performance and rate capability over pristine CoS. Additionally, this CoS/rGO can be a promising electrode material for supercapacitors as well as other power source devices.

ACKNOWLEDGMENT

REFERENCES

1. E.I. Gkanas and M. Khzouz, *Renew. Energy* 111, 484 (2017).
2. M.Y. Ho, P.S. Khiew, D. Isa, T.K. Tan, W.S. Chiu, and C.H. Chia, *Curr. Appl. Phys.* 14, 1564 (2014).
3. P. Sharma and T.S. Bhatti, *Energy Convers. Manag.* 51, 2901 (2010).
4. W.H. Zuo, R.Z. Li, C. Zhou, Y.Y. Li, J.L. Xia, and J.P. Liu, *Adv. Sci.* 4, 1600539 (2017).
5. M. Winter and R.J. Brodd, *Chem. Rev.* 104, 4245 (2004).
6. B.S. Singu, S.E. Hong, and K.R. Yoon, *J. Solid State Electrochem.* 21, 3215 (2017).
7. L. Khandare and S. Terdale, *Appl. Surf. Sci.* 418, 22 (2017).
8. F. Tao, Y.Q. Zhao, G.Q. Zhang, and H.L. Li, *Electrochem. Commun.* 9, 1282 (2007).
9. Y. Li, S.T. Liu, W. Chen, S. Li, L.L. Shi, and Y. Zhao, *J. Alloys Compd.* 712, 139 (2017).
10. C.K. Ranaweera, Z. Wang, E. Alqurashi, P.K. Kahol, P.R. Dvomic, B.K. Gupta, K. Ramasamy, A.D. Mohite, G. Gupta, and R.K. Gupta, *J. Mater. Chem. A* 4, 9014 (2016).
11. L. Zhang, H.B. Wu, and X.W. Lou, *Chem. Commun.* 48, 6912 (2012).
12. J.C. Xing, Y.L. Zhu, Q.W. Zhou, X.D. Zheng, and Q.J. Jiao, *Electrochim. Acta* 136, 550 (2014).
13. J.Y. Lin, Y.T. Tsai, S.Y. Tai, Y.T. Lin, C.C. Wan, Y.L. Tung, and Y.S. Wu, *J. Electrochem. Soc.* 160, D46 (2013).
14. C.J. Raj, M. Rajesh, R. Manikandan, J.Y. Sim, K.H. Yu, S.Y. Park, J.H. Song, and B.C. Kim, *Electrochim. Acta* 247, 949 (2017).
15. J.J. Zhang, Z.X. Chen, Y. Wang, and H. Li, *Energy* 113, 943 (2016).
16. X.M. Wu, Q.G. Wang, W.Z. Zhang, Y. Wang, and W.X. Chen, *Eletrochim. Acta* 211, 1066 (2016).
17. H.Y. Qin, S. Yang, W.L. Zhao, Z.C. Yang, X. Li, H.J. Li, and P. Yao, *Appl. Surf. Sci.* 420, 77 (2017).
18. Y.Y. Zheng, J. Xu, Y. Zhang, X.S. Yang, Y.J. Zhang, and Y.Y. Shang, *New J. Chem.* 42, 150 (2018).
19. S. Akbulut, M. Yilmaz, S. Raina, S.H. Hsu, and W.P. Kang, *J. Appl. Electrochem.* 47, 1035 (2017).
20. B.H. Qu, Y.J. Chen, M. Zhang, L.L. Hu, D.N. Lei, B.A. Lu, Q.H. Li, Y.G. Wang, L.B. Chen, and T.H. Wang, *Nanoscale* 4, 7810 (2012).
21. J.H. Shi, X.C. Li, G.H. He, L. Zhang, and M. Li, *J. Mater. Chem. A* 3, 20619 (2015).
22. Y. Wei, S.Y. Zhang, H.L. Niu, C.J. Mao, J.M. Song, B.K. Jin, and Y.P. Tian, *J. Wuhan Univ. Technol. Mater. Sci. Ed.* 32, 80 (2017).
23. Y. Wang, J. Tang, B. Kong, D.S. Jia, Y.H. Wang, T.C. An, L.J. Zhang, and G.F. Zheng, *RSC Adv.* 5, 6886 (2015).
24. W.S. Hummers and R.E. Offeman, *J. Am. Chem. Soc.* 80, 1339 (1958).
25. Y. Wang, Y.M. Li, L.H. Tang, J. Lu, and J.H. Li, *Electrochem. Commun.* 11, 889 (2009).
26. K. Dai, D.P. Li, L.H. Lu, Q. Liu, J.L. Lv, and G.P. Zhu, *RSC Adv.* 4, 29216 (2014).
27. W. Xiao, W. Zhou, Y. Zhang, L. Tian, H. Liu, and Y. Pu, *J. Nanomater.* 2016, 6201546 (2016).
28. G.C. Huang, T. Chen, Z. Wang, K. Chang, and W.X. Chen, *J. Power Sources* 235, 122 (2013).
29. A.C. Ferrari, *Solid State Commun.* 143, 47 (2007).
30. H.L. Lin, F. Liu, X.J. Wang, Y.N. Ai, Z.Q. Yao, L. Chu, S. Han, and X.D. Zhuang, *Electrochim. Acta* 191, 705 (2016).
31. L.L. Fan, X.F. Li, B. Yan, X.J. Li, D.B. Xiong, D.J. Li, H. Xu, X.F. Zhang, and X.L. Sun, *Appl. Energy* 175, 529 (2016).
32. C.Y. Chen, Z.Y. Shi, Z. Yang, and H.T. Chang, *J. Power Sources* 215, 43 (2012).
33. K.J. Huang, J.Z. Zhang, G.W. Shi, and Y.M. Liu, *Mater. Lett.* 131, 45 (2014).
34. C. Xu, Y. Jing, J.R. He, K.R. Zhou, Y.F. Chen, Q. Li, J. Lin, and W.L. Zhang, *J. Alloys Compd.* 708, 1178 (2017).
35. J. Zhu, Y. Wei, Y.Z. Zhou, and J. Yang, *Ceram. Int.* 44, 1836 (2018).
36. S. Zhang, C. Li, H.Q. Xiao, G.J. Wei, Y. Zhou, Z.J. Wang, J. Zhang, and C.H. An, *J. Nanopart. Res.* 19, 202 (2017).
37. F.L. Luo, J. Li, H.Y. Yuan, and D. Xiao, *Electrochim. Acta* 123, 183 (2014).
38. J. Zhu, L. Xiang, D. Xi, Y.Z. Zhou, and J. Yang, *Bull. Mater. Sci.* 41, 54 (2018).
39. C.Q. Zhang, Q.D. Chen, and H.B. Zhan, *ACS Appl. Mater. Interfaces* 8, 22977 (2016).
40. C. Jiang, B. Zhao, J.Y. Cheng, J.Q. Li, H.J. Zhang, Z.H. Tang, and J.H. Yang, *Electrochim. Acta* 173, 399 (2015).
41. J.W. Lee, T. Ahn, D. Soundararajan, J.M. Ko, and J.D. Kim, *Chem. Commun.* 47, 6305 (2011).
42. D. Ghosh and C.K. Das, *ACS Appl. Mater. Interfaces* 7, 1122 (2015).
43. X.M. Feng, N.N. Chen, J.H. Zhou, Y. Li, Z.D. Huang, L. Zhang, Y.W. Ma, L.H. Wang, and X.H. Yan, *New J. Chem.* 39, 2261 (2015).
44. X.M. Song, L.C. Tan, X.L. Wang, L. Zhu, X.Q. Yi, and Q. Dong, *J. Electroanal. Chem.* 794, 132 (2017).
45. T. Wu, J. Li, L. Hou, C. Yuan, L. Yang, and X. Zhang, *Electrochim. Acta* 81, 172 (2012).
46. K. Subramani, N. Sudhan, R. Divya, and M. Sathish, *RSC Adv.* 7, 6648 (2017).
47. J.Y. Ye, Z. Li, Z. Dai, Z.Y. Zhang, M.Q. Guo, and X.J. Wang, *J. Electron. Mater.* 45, 4237 (2016).
48. Y.A. Kumar, S.S. Rao, D. Punnoose, C.V. Tulasivarma, C. Gopi, K. Prabakar, H.J. Kim, and R. Soc, *Open Sci.* 4, 170427 (2018).
49. S.B. Kale, A.C. Lokhande, R.B. Pujari, and C.D. Lokhande, *J. Colloid Interface Sci.* 532, 491 (2018).
50. Q. Xu, D.L. Jiang, T.Y. Wang, S.C. Meng, and M. Chen, *RSC Adv.* 6, 55039 (2016).
51. Y.M. Fan, Y.C. Liu, X.B. Liu, Y.N. Liu, and L.Z. Fan, *Electrochim. Acta* 249, 1 (2017).
52. M. Shahraki, S. Elyasi, H. Heydari, and N. Dalir, *J. Electron. Mater.* 46, 4948 (2017).